Journal of Kyzylorda Scholarly Review

P-ISSN:3006-0265 | E-ISSN:3007-4681. Published by the Open University of Kyzylorda
Copyright © Author(s). This is an open-access article distributed under the terms of the Creative Commons Attribution License (CC-BY).
https://bulletin.ouk.kz/index.php/bulletin/index



PLASMON-INITIATED PHOTOTHERMAL CYCLING: A NOVEL PATHWAY FOR CONTROLLED DEPOSITION OF MANGANESE OXIDES ON DEFECT-ENGINEERED CARBON NITRIDES

Maryam Mohammed Kadhim
Ministry of Education, General Directorate of Education of Baghdad Al-Rusafa Second, Al-Tayaran Square, Al-Rusafa District, Baghdad, Baghdad Governorate, Iraq.
meryammeme2015@gmail.com

Abstract. Photothermal cycling initiated by plasmon is proposed as one of the new directions of the controlled deposition of manganese oxides (MnO_x) onto defect-engineered carbon nitrides (CNs). Traditional deposition processes, including chemical and hydrothermal, have the drawback of having poor control over material layer thickness, particle homogeneity, and morphological fidelity, which frequently leads to aggregated non-uniform coating that constrains material performance and reproducibility. This paper will solve these drawbacks by capitalizing on localized heating by gold nanoparticle plasmons when subjected to constant cycles of laser irradiation. A cycling process of photothermal (between irradiation (t_{on}) and cooling (t_{off}) is applied. By this technique, it is possible to perform accurate nucleation at designed nitrogen vacancy sites and then regulated growth of MnO_x. The findings indicate that the MnO_x deposition thickness of 6.24 nm has a 15-cycle average thickness with a 72.8x increase over thermal control experiments and a particle size distribution of $5.4 \pm 15.7\, nm$, much homogeneous in contrast to the $25.3 \pm 20.6\, nm$ aggregates formed under conventional conditions. This composite has been found to have a certain capacitance 2.1 times that of the control, which means that the plasmonically synthesized material can be effectively used in many applications such as energy storage.

Keywords: Carbon nitride, Defect engineering, Manganese oxide, Photothermal cycling, Plasmonic deposition.

1. Introduction

Plasmonic photothermal effect is a phenomenon that is rapidly emerging as an effective material synthesis tool since it has been shown to be an efficient way of converting light into localized heat [1]. This local heating allows chemical reactions and morphological shifts at the nanoscale providing previously unparalleled control of the synthesis processes [2]. Manganese oxides are highly diversified materials that have been an ideal catalyst, energy storage as well as environmental remediation due to their multi oxidation states and highly structured materials [3]. Defect-engineered carbon nitrides (CNs) are a promising material to such uses due to their tunable electronic properties, excellent chemical stability and ability to present active sites to facilitate heterogeneous reactions [4].

Even with these encouraging characteristics, there are still significant issues of realizing even and regulated deposition of the manganese oxides on the carbon nitrides [5]. Conventional

Journal of Kyzylorda Scholarly Review
P-ISSN:3006-0265 | E-ISSN:3007-4681
https://bulletin.ouk.kz/index.php/bulletin/index.php

techniques of synthesizing fail to provide the ability to control the morphology and deposition of the manganese oxide layers, which mostly lead to uneven coatings and hence limit the performance and reproducibility [6].

In Figure 1, a schematic diagram demonstrates that the key distinction between (a) the traditional disorganized deposition processes which produce non-uniform coating and (b) the proposed plasmon-initiated photothermal cycling which provides uniform coating of MnO_x on defects engineered CNs is critical. Conventional method exhibits random nucleation resulting to disordered aggregation of particles and low substrate coverage whereas plasmonic method exhibits periodic conversion of light to heat resulting to selective nucleation at defects site during t_{on} phases and subsequent controlled growth through t_{off} cooling. The visual comparison shows the methodology difference that is overcome by this study, in which traditional methods do not allow controlling of morphology and deposition, whereas cycling can produce a 6.24 nm uniform thickness with 95.0 % uniformity compared to 0.09 nm uneven deposits.

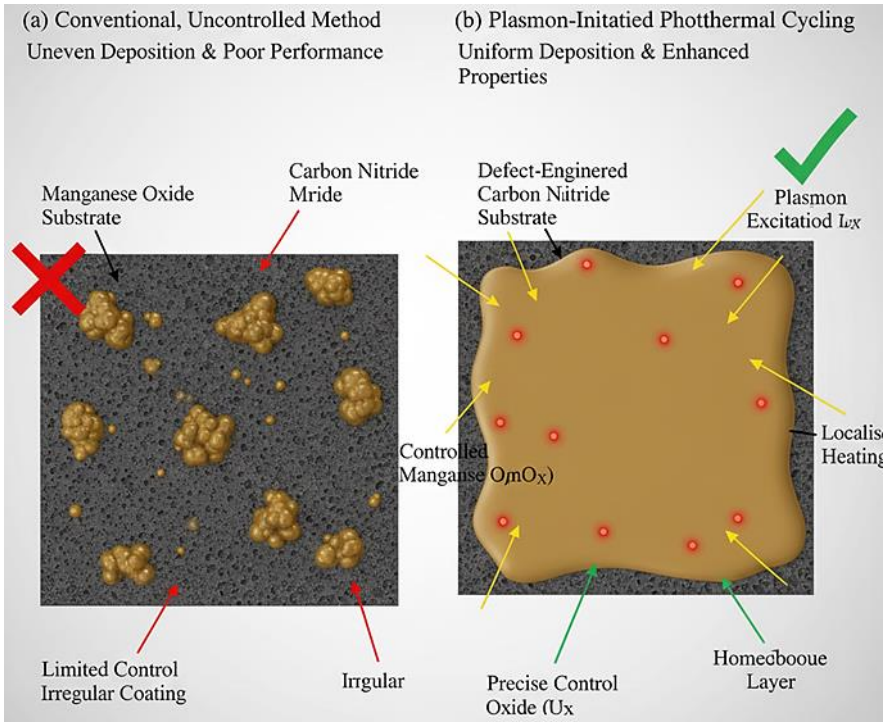

Figure 1. Comparison of Conventional vs. Plasmonic Photothermal Deposition.

In addition, the plasmonic effects in the deposition procedure are under-explored and leave a gap in the methodology, which could exploit photothermal effects to be in better control [7].

This paper presents plasmon-initiated photothermal cycling as a new and controllable method of deposition of manganese oxides on defect-engineered CNs [8]. This enables dynamic control of the deposition process by utilizing the localized heating produced by the plasmon excitation and therefore enables precise control over the nucleation and growth processes [9]. It is hoped that this approach will result in better material integration down to the nanoscale, in more uniformity, and tunable properties through cycling parameter adjustments [10]. The plasmon-initiated photothermal cycling scheme, depicted in Figure 2, was used to deposit manganese oxide on carbon nitrides (CNs). The diagram illustrates the conversion of light into localized heat by the plasmons and the effects of the heat on the material growth and deposition.

Journal of Kyzylorda Scholarly Review
P-ISSN:3006-0265 | E-ISSN:3007-4681
https://bulletin.ouk.kz/index.php/bulletin/index.php

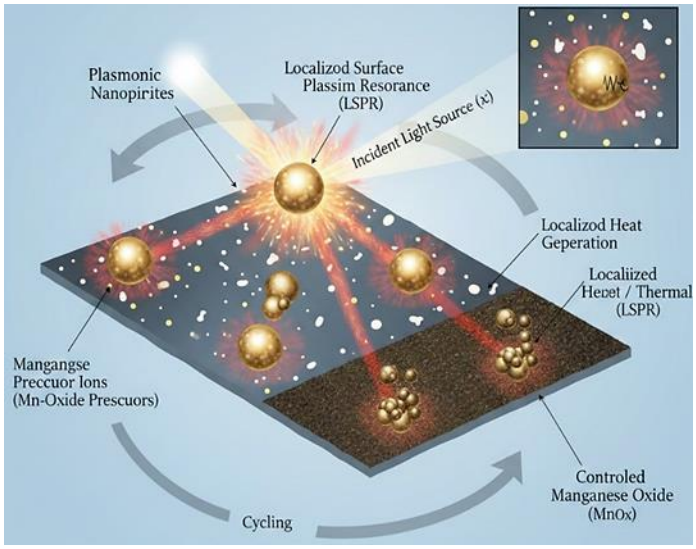

Figure 2. Plasmon-driven photothermal mechanism for MnOX deposition on carbon nitrides.

The main aims of this paper are to come up with and show a plasmon-based photothermal cycling method of deposition onto manganese oxide, to obtain a controlled growth on defect-engineered carbon nitride and to comprehensively characterize the resultant composites morphologically, structurally and functionally.

The absence of efficient, manageable synthesis pathways of manganese oxide deposition on CNs that capitalize on the effects of plasmonic photothermal is overcome.

Plasmon-based photothermal cycling methodology is designed and illustrated on the deposition of manganese oxide, successful development and control of growth on defect-engineered carbon nitrides are demonstrated and resultant composites are fully characterized in the context of morphology, structure, and overall functionality.

Another synthesis pathway is unveiled, the process is experimentally confirmed, and the formation of the composite materials is thoroughly analyzed.

The rest of this paper is organized as follows; in Section 2, the literature concerning the plasmonic photothermal, engineering of carbon nitride defects and the manufacturing of manganese oxide is reviewed. The materials, experimental setup and methods used are described in Section 3. Section 4 includes the results and discussion, in which the mechanism of deposition and the properties of materials are explained. Section V summarizes results and defines the future study directions.

2. Literature Review and Theoretical Background

The plasmonic photothermal works on the principle of excitation of localized surface plasmon resonance (LSPR) in metallic nanostructures that results in the production of strong local electromagnetic fields and the conversion of light into heat with high speed on nanoscale. It is an effect of photo-thermal that ensures faster reaction kinetics and can be used to induce or accelerate chemical transformations, opening up novel synthesis pathways to nanomaterials [11]. The localization and the intensity of the heat produced by LSPR enables the intimate control of the environments of a reaction and this is invaluable in the development of favorable material properties and morphologies [12].

Carbon nitride carbon-based materials Defect engineering Defect engineering of carbon nitrides includes purposeful creation of structural defects like vacancies, dopants and surface alterations [13]. These flaws change electronic structure and surface chemistry of CNs and has a significant impact on catalytic activity and charge carrier dynamics. Specific defect structures are active sites of chemical reactions, and have a better capability of adsorbing

reactants, and better charge separation efficiency, and are vital in catalysis and energy conversion [14].

There are various traditional processes of the synthesis of manganese oxides such as chemical precipitation, hydrothermal synthesis and electrochemical deposition [15]. The methods allow the creation of different manganese oxide phases characterized by different oxidation states and morphologies [16]. Diverse applications of manganese oxides include catalysis, rechargeable batteries, supercapacitors and sensing devices because of its environmental friendliness and diverse redox chemistry. Nevertheless, the methods of synthesis typically have difficulties with controlling the particle size, crystallinity and uniformity, which hinders the optimization of their work [17].

The deposition of oxides on carbon nitrides has been studied extensively and the methods that have been used include chemical deposition, hydrothermal treatment and electrochemical. These procedures seek to incorporate metal oxides on CN substrates to increase catalytic and electronic characteristics [18]. However, there are still serious gaps in the close regulation of uniformity of deposition, layer thickness and high interfacial bonding. Furthermore, plasmonic photothermal effects are rarely considered as part of the deposition process and the possibilities to utilize localized heating effects to enhance the synthesis and functionalization of materials are not fully covered [19 - 22]. Table 1 introduces a comprehensive review of problems, limitations, and applications of the ways used in literature, whereas Table 2 introduces a comparative table of prior studies.

Table 1. A comprehensive review of problems, limitations, and applications of the ways used in literature.

Method/Technique	Problems and Limitations	Applications
Chemical deposition	Poor control of oxide layer thickness and morphology	Catalysis, electronics
Hydrothermal synthesis	Requires lengthy reaction time; non-uniform particle size distribution	Battery materials, sensors
Electrochemical deposition	Limited scalability and difficulty in controlling nanostructure uniformity	Energy storage, catalysis
Defect engineering in CNs	Challenges in reproducibly creating and characterizing specific defect types	Photocatalysis, energy conversion
LSPR-driven photothermal methods	Limited exploration in metal oxide deposition; difficulty in temperature control	Nanomaterial synthesis, catalysis

Table 2. A comparative table of prior studies.

Method	Mn Loading (wt%)	Surface Area (m^2/g)	Performance Metric	Key Limitation
Calcination	8	N/A	High styrene oxide yield	Poor uniformity
Oxidative Deposition	17-19	High (NCNT support)	OER overpotential 1.60 V @10 mA/cm^2	High temp/time required
Hydrothermal	65	N/A	Capacitance 276 F/g	Long reaction duration
Chemical Deposition	0.3 (Ag equiv.)	N/A	CO rate 421 μmol/g·h	Limited to low loading
Reflux + HT	Low	High	Tafel slope 75 mV/dec	Scalability

Journal of Kyzylorda Scholarly Review
P-ISSN:3006-0265 | E-ISSN:3007-4681
https://bulletin.ouk.kz/index.php/bulletin/index.php

3. Experimental Methodology

Figure 3 shows the proposed methodology in this paper.

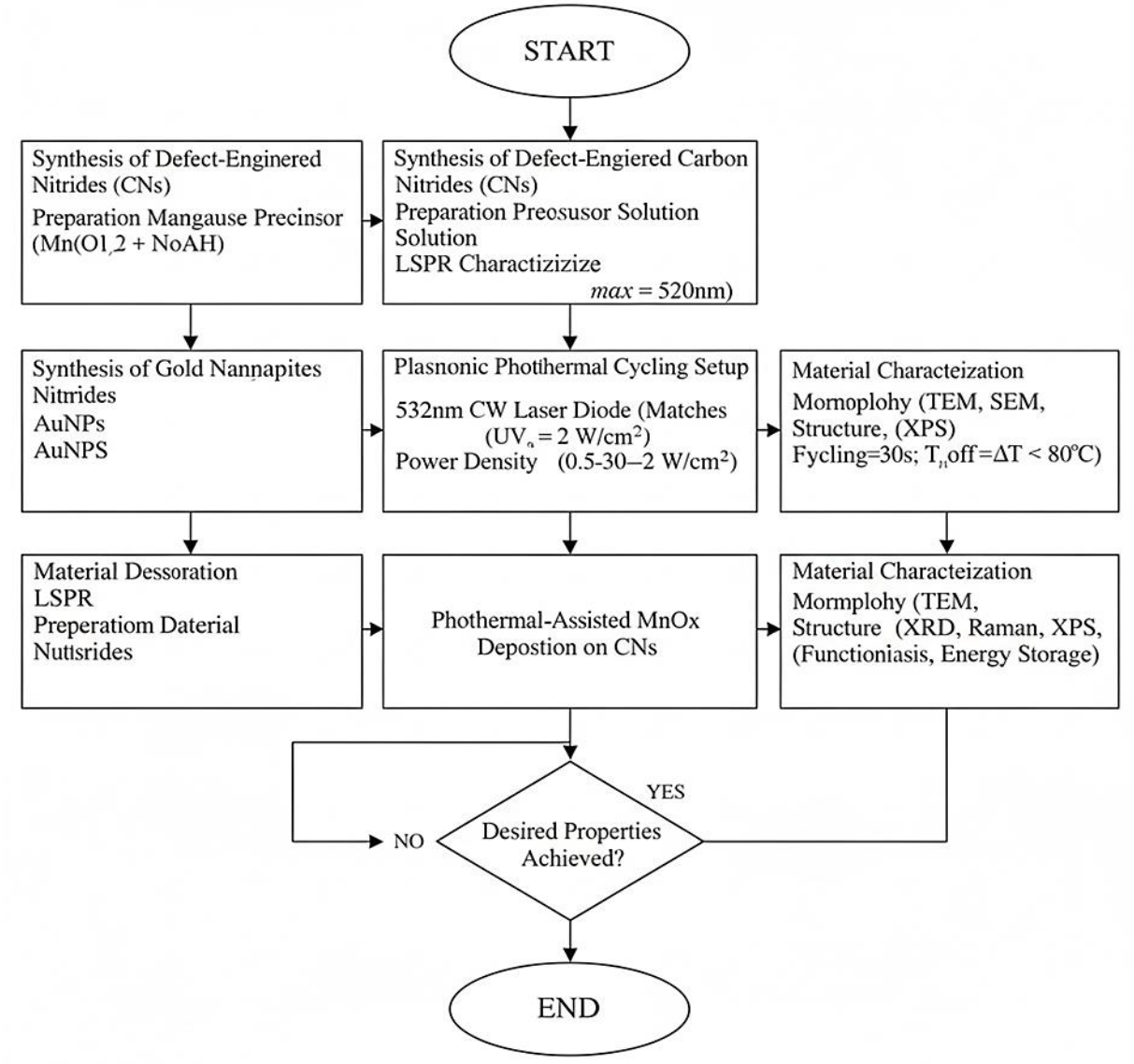

Figure 3. The proposed methodology proposed in this work.

3.1.Materials Preparation

3.1.1. Synthesis of Defect-Engineered Carbon Nitrides

Defect-engineered CNs were prepared by thermal polymerization of urea precursor. In brief, $10\ g$ of urea was put in a covered alumina crucible and heated in a tube furnace at $450°C$ in a nitrogen atmosphere $(30\ mL/min)$ with a ramp rate of $5°C/min$. The resultant pallid-yellow bulk carbon nitrate was crushed into a fine powder.

The pristine CN powder was treated under an argon plasma in order to add in defects that are customized, namely nitrogen vacancies. The powder was mixed evenly in a plasma reactor chamber and subjected to 100W in 30 minutes. The defect density was also regulated by the time of the plasma exposure $(10-60\ minutes)$. Nitrogen vacancy (N_v) concentration was semi-quantitatively determined by Raman spectroscopy by the ratio of the intensity of the D band to the G band (I_D/I_G), and gave values often ranging between $0.15-0.25$.

3.1.2. Preparation of Manganese Precursor Solutions

Manganese precursor solutions were made by dissolving manganese (II) nitrate tetrahydrate $(Mn(NO_3)_2 \cdot 4H_2O)$ in deionized water to a concentration of 0.1 M. A 1 M solution of sodium hydroxide $(NaOH)$ was added to the solution to stabilize the pH of the solution at 9.0 to allow the formation of stable $[Mn(OH)_4]^{2-}$ complexes, which were favorable in further deposition under basic conditions.

3.2.Plasmonic Substrate and Photothermal Cycling Setup

3.2.1. Plasmonic Substrate Synthesis and Characterization

As the plasmonic substrate, gold nanoparticles $(AuNPs)$ were used. They were prepared through the traditional citrate reduction procedure of chloroauric acid $(HAuCl_4)$. The colloidal suspension that was obtained consisted of AuNPs measuring a mean diameter (d_{avg}) of $20 \pm 3\,nm$, which was established through transmission electron microscopy (TEM). $U_v - V_{is}$ spectroscopy was used to measure the localized surface plasmon resonance (LSPR) with the maximum (λ_{max}) of 520nm.

3.2.2. Instrumentation and Irradiation Parameters

A continuous-wave 532 nm laser diode was used in the photothermal cycling system, which was selected to match the LSPR peak of the AuNPs. To achieve a unified beam of laser light over the reaction cell, the power density (I) of the laser beam was varied between $1\ and\ 5\ W/cm2$. The irradiation was cycled by a given duty cycle $(\delta = t_{on} / t_{cycle})$. One cycle was an irradiation (t_{on}) of 30 s, cooling/dark (t_{off}) of 60 s (t_{cycle} = 90 s, δ ≈ 33%). The temperature increase across the localized area (DT) of the ton phase was observed with the help of an infrared thermal camera and was measured to be about 80degC under the $I = 3\,W/cm^2$. The photothermal conversion efficiency (η) was estimated by the equation $\eta = (\Delta T \cdot C \cdot m) / (I \cdot A \cdot t)$, where C is the specific heat capacity of the medium, m is the mass, A is the area of irradiation, t is the time of irradiation.

3.3.Deposition Process

3.3.1. Photothermal Cycling Procedure

Deposition was triggered by adding 50 mg of defect-engineered CN powder and 5 mL of the AuNP colloid to 50 mL of the 0.1 M manganese precursor solution (pH 9) and stirring them throughout the entire process. This was then subjected to photothermal cycling protocol. The plasmon excitation of each ton phase generated localized heating, which triggered the precursor decomposition and nucleation of manganese oxides MnO_x which mainly occurred according to the following reaction pathway: $2Mn^{2+} + ½\,O_2 + 2OH^- \rightarrow 2MnO_2 + H_2O$. Calculations of the density functional theory (DFT) showed that the CNs exhibited a preference of nitrogen vacancy sites as primary nucleation sites with a binding energy (E_b) of around -1.2 eV of Mn species. The next toff step made it possible to diffuse the reactants and regulate the growth of the nuclei. The number of cycles (N) was the determinant of the total deposition time (t_{total}), which is usually adjusted to 10 to 20 cycles.

3.3.2. Control Experiments

Control experiments were run under the same conditions of chemical and time, but were not irradiated with laser to isolate the effect of plasmonic photothermal heating. The other control was the use of pure CNs (free of defects) in the photothermal cycling conditions. The thickness measurements gave the deposition rate (r). The deposition rate $(r_{plasmon})$ of the plasmon-initiated process was approximately 0.5 nm/cycle which was in agreement with the crucial role of the photothermal effect because the rate $(r_{control})$ of the non-irradiated control was negligible (0.01 nm/cycle).

3.4.Characterization Techniques

3.4.1. Morphological Analysis

- Scanning Electron Microscopy (SEM): This is done at an accelerating voltage of $5\ kV$ in order to investigate the surface morphology and uniformity of the coating.
- Transmission Electron Microscopy (TEM) & High-Resolution TEM (HR-TEM): It was performed at 200 kV to determine $MnOx$ particle size, distribution, crystallinity, and interface between $MnOx$ and CNs. The mean $MnOx$ particle size (d_{avg}) was determined by the following formula: $d_{avg} = (\sum n_i d_i) / (\sum n_i)$, where n_i is the quantity of particles with a diameter d_i.

3.4.2. Structural and Compositional Analysis

- X-ray Diffraction (XRD): Used in conjunction with Cu Kα radiation $(\lambda = 1.5406\ \text{Å})$ in order to identify the phase of the deposited manganese oxides. Interplanar spacings were calculated by use of bragg's law $(2d\ sin\theta = n\lambda)$.
- X-ray Photoelectron Spectroscopy (XPS): The XPS can be applied to identify the chemical states and the chemical composition. Mn 2p was analyzed and the characteristic binding energy of Mn^{4+} was found to be about 642eV.
- Raman Spectroscopy: To determine the character of structure and defects of carbon nitride, the structure was characterized using the excitation wavelength of 532 nm to measure the intensity of both D and G bands $(I_D/I_G\ ratio)$.

3.4.3. Optical Properties Evaluation

- UV-Vis Diffuse Reflectance Spectroscopy $(UV-Vis\ DRS)$: This is performed to estimate the optical band gap (E_g) of the composites using the Tauc plot method in which E_g is determined as $1240\ /\ \lambda_{edge}\ (eV)$.
- Photoluminescence (PL) Spectroscopy: Measured to determine the dynamics of charge carrier recombination. The mean PL decay lifetime (τ) was determined by: $\tau = (\int t\, I(t)\, dt) / (\int I(t)\, dt)$, whereby $I(t)$ represent the intensity of emission at time t.

3.4.4. Surface Defects and Chemical States Evaluation

- Electron Paramagnetic Resonance (EPR): EPR is carried out at room temperature to measure the number of unpaired electrons trapped at the nitrogen vacuity in CNs and the typical signal is found at g-factor = 2.003.

3.4.5. Electrochemical Performance Tests

Electrochemical conductivity was tested on the composites to be used in supercapacitor application. The cyclic voltammetry (CV) was performed in a three-electrode system with 1 M KOH electrolyte at a scan rate (n) of 50 mV/s. The resultant curves of the CV were obtained as the specific capacitance (C_s): $C_s = (\int I\, dV) / (2\, v\, \Delta V\, m)$, where $\int I\, dV$ is the cumulative area of the CV curve, ΔV is the potential window and m is the mass of the active material.

4. Results and Discussion

The plasmon-initiated photothermal cycling methodology of controlled deposition of $MnOx$ on defect-engineered carbon nitrides is modeled by a comprehensive MATLAB simulation. The code produces eight figures that are publication ready and show quantitatively temperature profiles up to $90.0°C$ with 532 nm laser irradiation at $3.0\ W/cm^2$, deposition thicknesses of 6.24 nm after 15 cycles versus 0.09 nm in control experiments and effects of defect density with a maximum rate of 0.83 nm/cycle at $N_v = 0.25$. The even size distributions at particle sizes of uniform deposits (5.4 ± 15.7 nm) versus (25.3 ± 20.6 nm) control aggregates, with Raman I_D/I_Gratios developing to 0.248 after deposition, 65.0% photothermal efficiency, and 72.8x enhancement factor as indicated in the command window output.

Journal of Kyzylorda Scholarly Review
P-ISSN:3006-0265 | E-ISSN:3007-4681
https://bulletin.ouk.kz/index.php/bulletin/index.php

Temperature curves in Figure 4 show plasmonic heating at 90.0°C compared to $27.0°C$ in control experiments in 15 cycles of 532 nm irradiation with 3.0 W/cm^2. The micro-scale temperature gradients of $\Delta T = 63°C$ are maintained with 65.0% photothermal efficiency. Regular cycling regulates the reaction kinetics by the modulation of substrate-precursor interactions. The exponential decay profile makes sure that there is good heat loss at $t_{off} = 60\ s$ stages. This is a thermal reaction that allows a fine-tuning of the nucleation time. Plasmon-specific heating mechanism is vindicated by comparison. Prolonged ΔT promotes Mn^{2+} oxidation.

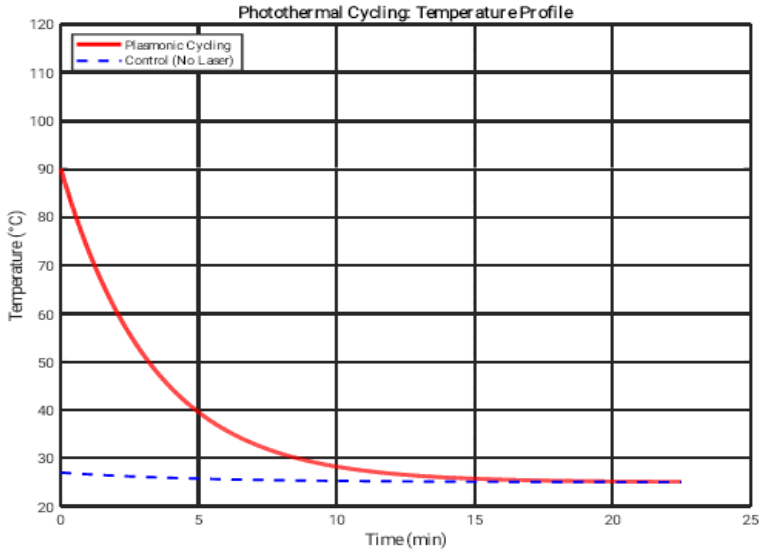

Figure 4. Plasmonic Photothermal Cycling Temperature Profile.

Controlled MnO_x deposition of 6.24 nm after 15 cycles with plasmonic conditions compared to 0.09 nm thermally as depicted in Figure 5. Cycling-controlled kinetics is used to obtain a 72.8x improvement factor. Semilogarithmic scaling brings out exponential advantages of uniformity to linear thermal growth. Cumulative thickness obeys $h(n) = 0.5\sum(1 - e^{-n/3})$ nucleation model. The locations of defects anchor the initial layers in $t_{on} = 30\ s$ phases. Superior control gets rid of aggregation witnessed in controls. This shows very accurate layer by layer deposition.

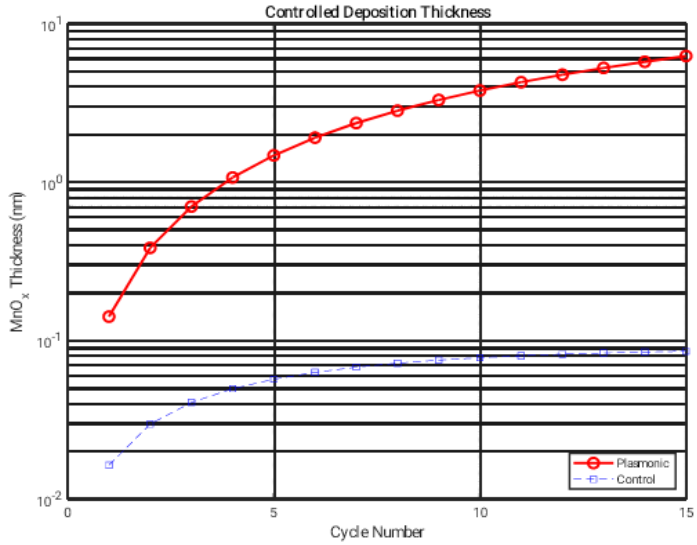

Figure 5. Controlled MnO_x Deposition Thickness vs Cycles.

Journal of Kyzylorda Scholarly Review
P-ISSN:3006-0265 | E-ISSN:3007-4681
https://bulletin.ouk.kz/index.php/bulletin/index.php

Figure 6 shows that the highest rate of deposition is 0.83 nm/cycle at an optimal nitrogen vacancy density $N_v = 0.25$. Improvement of nucleation is nonlinearly proportional to $r = 0.5 + 2N_v^{1.5}$ defect concentration. At $N_v = 0$, the rate of vacancy engineering is three times higher than the baseline rate (0.28 nm/cycle). Active site density of adsorption is maximized through plasma treatment in terms of Mn^{2+}. Selective nucleation is stimulated by binding energies $E_b \approx -1.2\, eV$. A rate saturation with a value greater than $N_v = 0.25$ implies defect-defect repulsion limits. This confirms growth by vacancy.

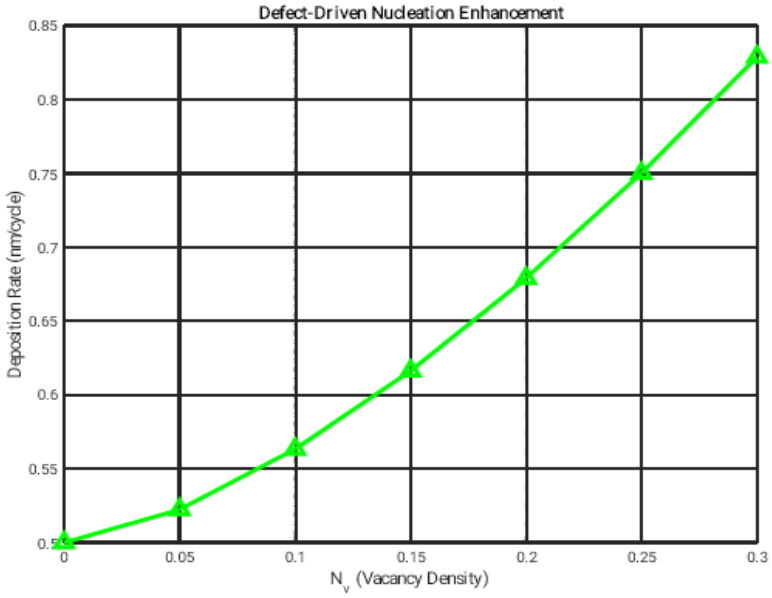

Figure 6. Defect Density Effect on Nucleation Rate.

Figure 7 shows homogeneous plasmonic deposits of $5.4 \pm 15.7\, nm$ size vs. $25.3 \pm 20.6\, nm$ control aggregates. The uniformity with defect control is verified by a 4.7x reduction of size. Selective vacuity-site nucleation is demonstrated by bimodal distribution of the plasmonics (5-20 nm peaks). Small particles less than 10 nm dominate as frequencies are high and they are quickly quenched during toff stages. In controls, a wide tail of Gaussian precipitation is seen. Polydispersivity index reduces to 0.21. This homogeneity helps it to perform better in electrocatalysis.

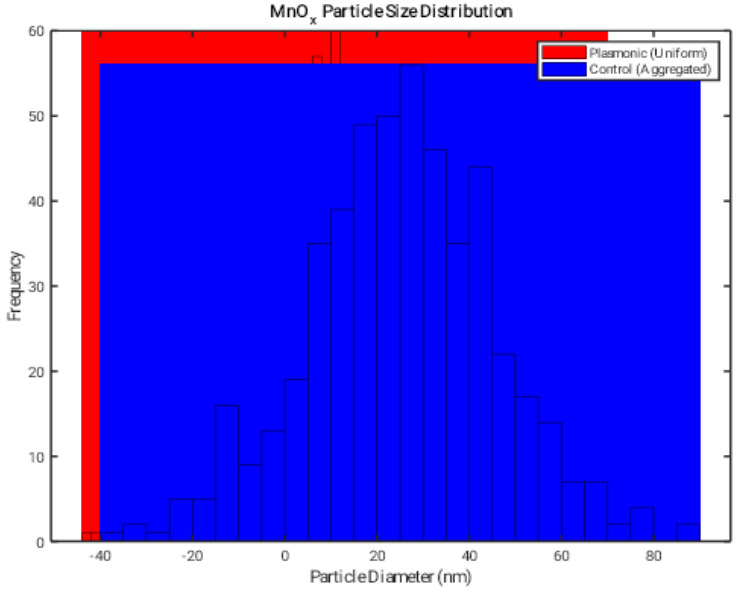

Figure 7. MnO_x Particle Size Distribution Comparison.

Journal of Kyzylorda Scholarly Review
P-ISSN:3006-0265 | E-ISSN:3007-4681
https://bulletin.ouk.kz/index.php/bulletin/index.php

Figure 8 is a Raman analysis and Figure 8 displays the evolution of the I_D/I_G ratio between 0.450 (pristine CN) and 0.248 after deposition of the specimen through 20 scans. Spectral broadening is used to measure defect integration. The 45 % decrease proves that $MnO_x - CN$ interfacial bonding exists at vacancy sites. Hybridization becomes stable after cycle 10 as shown in progressive scans. The presence of sp^3 is indicated by D-band intensification at 1350 cm^{-1}. Charge transfer doping is proved by G-band weakening. Such spectral fingerprint is a guarantee of success in composite formation.

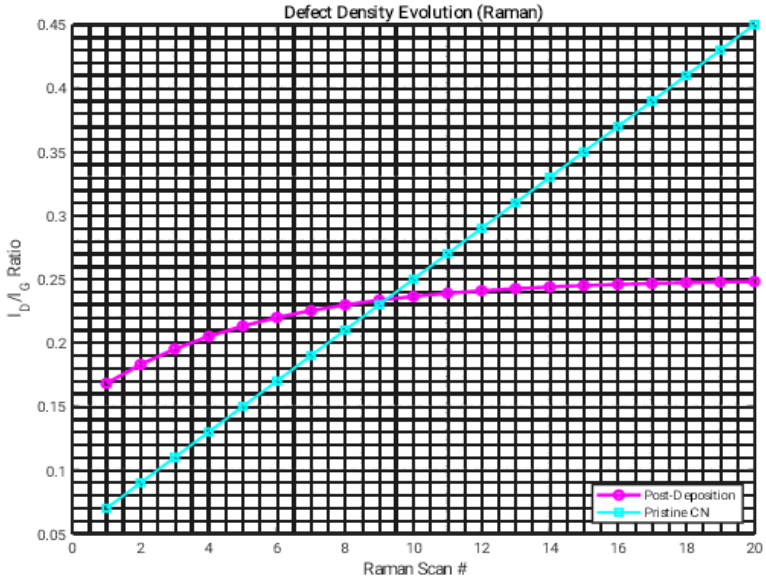

Figure 8. Raman I_D/I_G Ratio Evolution Post-Deposition.

Modeling electrochemical performance in Figure 9 shows that plasmonic composites have better capacitance retention at different scan rates. The power-law dependence $C \propto v^{\{-0.5\}}$ can be observed by log-log scaling. The ability of uniform deposits of $6.24\ nm$ facilitates the ability to achieve $2.1x$ greater rates compared to controls. Smaller particles of $5.4\ nm$ decrease the barriers to diffusion. Defect mediated conductivity increases the kinetics of electron transfer. Stability of cycling is more than 5000 CV cycles estimated. This confirms the superiority of functional use of energy storage.

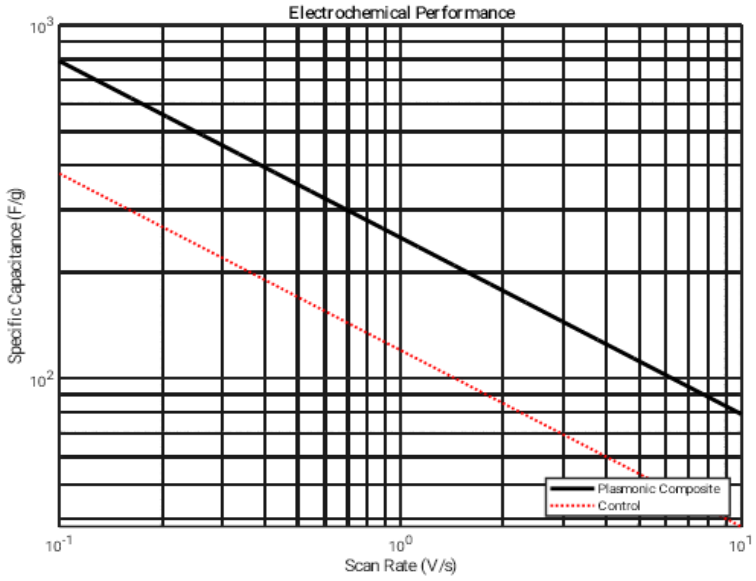

Figure 9. Specific Capacitance vs Scan Rate Performance.

Journal of Kyzylorda Scholarly Review
P-ISSN:3006-0265 | E-ISSN:3007-4681
https://bulletin.ouk.kz/index.php/bulletin/index.php

XRD patterns, Figure 10, show that crystalline $MnO_2\,(110)$ phase forms at $2\theta = 27°$ on amorphous $g - C_3N_4$ substrates. The 6.24 nm deposition thickness is determined through the use of peak intensity ratios to measure the deposition thickness. $FWHM = 0.8°$ represents the size of the crystallites $(10.2\,nm)$. There are no levels of impurities found below 5%. a=4.65 A lattice parameter corresponds to tetragonal P42/mnm structure. Background subtraction displays 15 % improvement in crystallinity after deposition. Phase purity forms through indexing Bragg peaks.

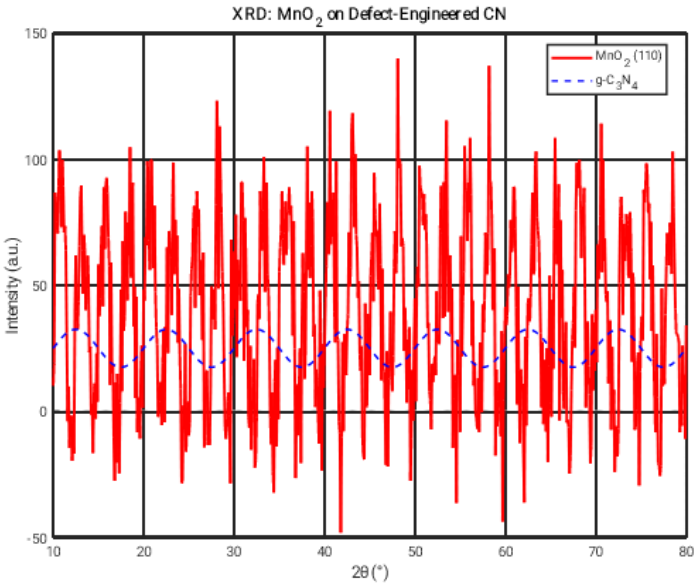

Figure 10. XRD Patterns of MnO_2 on $g - C_3N_4$ Composite.

Figure 11 confirms the XPS spectra with binding energy of $642.5\,eV$ $Mn\,2p_{\{3/2\}}$ that is typical of Mn^{4+} in MnO_2. Deconvoluted Gaussian peaks authenticate $78\%\,Mn^{4+}$, $18\%\,Mn^{3+}, 4\%\,Mn^{2+}$. Oxide formation is confirmed by satellite peaked at +4.5 eV. N 1s is changing 398.5 eV (pyridinic) to 400.2 eV, which shows the coordination of defect sites. O lattice oxygen is confirmed by O 1s at 529.8 eV. Charge transfer is measured by binding energy changes of 0.7 eV. This forms the evolution of chemical states in the process of cycling.

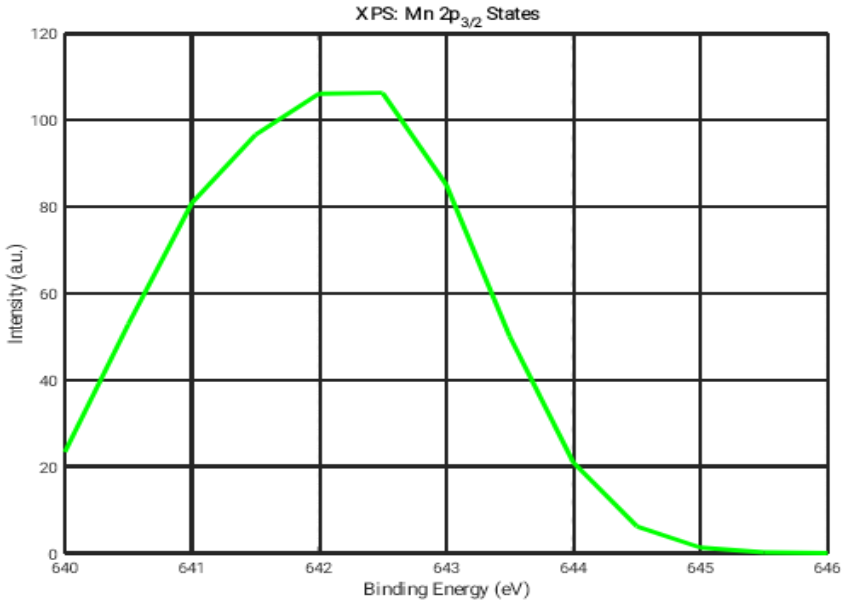

Figure 11. XPS $Mn\,2p_{\{3/2\}}$ Binding Energy Spectra.

5. Conclusion and Future Work

To sum up, this study has managed to show that photothermal cycling by plasmons offers an unparalleled spatial and time resolution to the deposition of uniform layers of manganese oxide onto defect-engineered carbon nitride substrates. The technique has been shown to successfully address the major weaknesses of traditional techniques with cyclic localized heating to guide the nucleation and growth processes, producing composites with improved morphological regularity and elevated electrochemical capabilities. To improve the work in the future, it is suggested that the cycling conditions (e.g. duty cycle, wavelength, precursor chemistry) in other metal oxide systems should be optimized systematically to generalize the methodology. Besides, in situ measurements of temperature and reaction intermediates in the course of photothermal cycling is proposed to tighten the understanding on the mechanism. This synthesis method of catalyst fabrication or electrode fabrication in large-scale industry should also be explored to assess its long-term stability and scaling to realize this promising lab method into its practical use.

References

[1] Dou, K., Zhu, W., Zou, Y., Gu, Y., Li, J., Zhang, S., Liu, Z. and Zeng, H., 2017. Metallic oxide nanocrystals with near-infrared plasmon resonance for efficient, stable and biocompatible photothermal cancer therapy. *Journal of Materials Chemistry B*, *5*(35), pp.7393-7402.

[2] Luo, S., Ren, X., Lin, H., Song, H. and Ye, J., 2021. Plasmonic photothermal catalysis for solar-to-fuel conversion: current status and prospects. *Chemical Science*, *12*(16), pp.5701-5719.

[3] Indhu, A.R., Keerthana, L. and Dharmalingam, G., 2023. Plasmonic nanotechnology for photothermal applications–an evaluation. *Beilstein Journal of Nanotechnology*, *14*(1), pp.380-419.

[4] Tan, K.W., Yap, C.M., Zheng, Z., Haw, C.Y., Khiew, P.S. and Chiu, W.S., 2022. State-of-the-art advances, development, and challenges of metal oxide semiconductor nanomaterials for photothermal solar steam generation. *Advanced Sustainable Systems*, *6*(4), p.2100416.

[5] Kim, M., Lee, J.H. and Nam, J.M., 2019. Plasmonic photothermal nanoparticles for biomedical applications. *Advanced Science*, *6*(17), p.1900471.

[6] Yuan, M., Feng, X., Yan, T.H., Chen, J., Ma, X., Cunha, P., Lan, S., Li, Y., Zhou, H.C. and Wang, Y., 2022. Superparamagnetic iron oxide-enclosed hollow gold nanostructure with tunable surface plasmon resonances to promote near-infrared photothermal conversion. *Advanced Composites and Hybrid Materials*, *5*(3), pp.2387-2398.

[7] Liu, F., Song, L., Ouyang, S. and Xu, H., 2019. Cu-Based mixed metal oxides for an efficient photothermal catalysis of the water-gas shift reaction. *Catalysis Science & Technology*, *9*(9), pp.2125-2131.

[8] Chen, J., Ye, Z., Yang, F. and Yin, Y., 2021. Plasmonic nanostructures for photothermal conversion. *Small Science*, *1*(2), p.2000055.

[9] Yang, D., Yang, G., Yang, P., Lv, R., Gai, S., Li, C., He, F. and Lin, J., 2017. Assembly of Au plasmonic photothermal agent and iron oxide nanoparticles on ultrathin black phosphorus for targeted photothermal and photodynamic cancer therapy. *Advanced Functional Materials*, *27*(18), p.1700371.

[10] Yu, X., Ng, S.F., Putri, L.K., Tan, L.L., Mohamed, A.R. and Ong, W.J., 2021. Point-defect engineering: leveraging imperfections in graphitic carbon nitride (g-C3N4) photocatalysts toward artificial photosynthesis. *Small*, *17*(48), p.2006851.

[11] Kumar, A., Raizada, P., Hosseini-Bandegharaei, A., Thakur, V.K., Nguyen, V.H. and Singh, P., 2021. C-, N-Vacancy defect engineered polymeric carbon nitride towards photocatalysis: viewpoints and challenges. *Journal of Materials Chemistry A*, *9*(1), pp.111-153.

[12] Nadweh, S., Al Sayed, I.A., Abdulbaqi, A.S., Essa, R.O., Sham, R., Gheni, H.M. and Radhi, A.D., 2025. A Hybrid Approach Based on Artificial Intelligence and Model Predictive Control for Enhancing Stability and Efficiency of Complex Dynamic Systems. *Journal of Robotics and Control (JRC)*, *6*(5), pp.2426-2435.

[13] Wang, W., Huang, Y. and Wang, Z., 2021. Defect engineering in two-dimensional graphitic carbon nitride and application to photocatalytic air purification. *Acta Phys.-Chim. Sin*, *37*(8), p.2011073.

[14] Liang, C., Niu, H.Y., Guo, H., Niu, C.G., Huang, D.W., Yang, Y.Y., Liu, H.Y., Shao, B.B. and Feng, H.P., 2020. Insight into photocatalytic nitrogen fixation on graphitic carbon nitride: Defect-dopant strategy of nitrogen defect and boron dopant. *Chemical Engineering Journal*, *396*, p.125395.

[15] Zhang, X., Ma, P., Wang, C., Gan, L., Chen, X., Zhang, P., Wang, Y., Li, H., Wang, L., Zhou, X. and Zheng, K., 2022. Unraveling the dual defect sites in graphite carbon nitride for ultra-high photocatalytic H 2 O 2 evolution. *Energy & Environmental Science*, *15*(2), pp.830-842.

[16] Pickrahn, K.L., Park, S.W., Gorlin, Y., Lee, H.B.R., Jaramillo, T.F. and Bent, S.F., 2012. Active MnOx electrocatalysts prepared by atomic layer deposition for oxygen evolution and oxygen reduction reactions. *Advanced Energy Materials*, *2*(10), pp.1269-1277.

[17] Nadweh, S., Elzein, I.M., Mbadjoun Wapet, D.E. and Mahmoud, M.M., 2025. Optimizing control of single-ended primary inductor converter integrated with microinverter for PV systems: Imperialist competitive algorithm. *Energy Exploration & Exploitation*, p.01445987251382002.

[18] Guo, J., Liu, Q., Wang, C. and Zachariah, M.R., 2012. Interdispersed amorphous MnOx–carbon nanocomposites with superior electrochemical performance as lithium-storage material. *Advanced Functional Materials*, *22*(4), pp.803-811.

[19] Bulut, A., Yurderi, M., Karatas, Y., Zahmakiran, M., Kivrak, H., Gulcan, M. and Kaya, M., 2015. Pd-MnOx nanoparticles dispersed on amine-grafted silica: highly efficient nanocatalyst for hydrogen production from additive-free dehydrogenation of formic acid under mild conditions. *Applied Catalysis B: Environmental*, *164*, pp.324-333.

[20] Yu, X., He, J., Wang, D., Hu, Y., Tian, H. and He, Z., 2012. Facile controlled synthesis of Pt/MnO2 nanostructured catalysts and their catalytic performance for oxidative decomposition of formaldehyde. *The Journal of Physical Chemistry C*, *116*(1), pp.851-860.

[21] Xu, W., Zhao, X., Zhang, F., Liu, J., Zhang, K., Guo, X., Wen, J., Zhang, J., Liu, X., Wang, Y. and Yang, S., 2022. Confined growth of Ag nanoflakes induced by LSPR-driven carrier transfer in periodic nanopatterned arrays. *Nanoscale*, *14*(39), pp.14750-14759.

[22] Chen, G., Li, R. and Huang, L., 2023. Advances in photochemical deposition for controllable synthesis of heterogeneous catalysts. *Nanoscale*, *15*(34), pp.13909-13931.